

DETECTING THE GROWTH OF STRUCTURES IN PURE STELLAR DISK MODELS

D. Valencia-Enríquez,¹ I. Puerari,¹ L. Chaves-Velasquez¹

Draft version: October 23, 2018

RESUMEN

Se ejecutaron simulaciones de N-cuerpos en 3D donde las condiciones iniciales fueron escogidas para obtener dos conjuntos de modelos; no-barrados y barrados. Aquí, Se analiza el crecimiento de las estructuras espirales y/o barra usando métodos de Transformada de Fourier 1D y 2D. Los espectrogramas y los diagramas de la amplitud de los coeficientes de Fourier en función del tiempo, radio y ángulo de enrollamiento muestra que la morfología de nuestros modelos es devida a la superposición de diversas estructuras con valores diferentes para el ángulo de enrollamiento, número de brazos y velocidad angular. Además, en los modelos donde se forma una barra, se estudió las órbitas de las partículas en el sistema de referencia de esta. Una clasificación geométrica de las órbitas muestra que el potencial de la barra y los puntos Lagrangianos L_4 y L_5 capturan aproximadamente 1/3 de la masa total del disco.

ABSTRACT

We performed a series of 3D N-body simulations where the initial conditions were chosen to get two sets of models; unbarred and barred ones. In this work, we analyze the growth of spirals and bar structures using 1D, and 2D Fourier Transforms FT methods. Spectrograms and diagrams of the amplitude of the Fourier coefficients as a function of time, radius and pitch angle show that the general morphology, of our modeled galaxies, is due to the superposition of structures which have different values of pitch angle and number of arms. Also, we made in barred models a geometric classification of orbits from the bar reference frame showing that the barred potential and the Lagrangian points L_4 and L_5 catch approximately one-third of the total disk mass.

Key Words: galaxies: kinematics and dynamics — galaxies: spiral — galaxies: structure — methods: numerical

1. INTRODUCTION

The physical origin and the evolution of non-axisymmetric structures in disk galaxies are long-standing problems in Astrophysics. One of the most widely accepted hypothesis is the Spiral Density Wave Theory (e.g. Lin & Shu 1964; Bertin & Lin 1996). In this theory, the spiral arms are explained as long-lived quasi-stationary density waves with a constant pattern speed. Additionally, Bertin & Lin (1996) introduced the supposition that these waves are the result of global modes. Their global mode analysis shows that the spiral arms

¹Instituto Nacional de Astrofísica, Óptica y Electrónica, INAOE, México.

are manifestations of the gravitationally unstable global eigen-oscillations of the disk galaxies (Dobbs & Baba 2014). Goldreich & Lynden-Bell (1965), Julian & Toomre (1966) and Toomre (1981) proposed that the spiral arms be stochastically produced by local gravitational perturbations in a differentially rotating disk: short leading spiral perturbation shears at corotation into a short trailing spiral due to the differential rotation. The wave is amplified by self-gravity of the assembly of stars at the perturbation. This mechanism is known as swing-amplification, and the resulting spiral structure is short lived (Toomre 1981). Masset & Tagger (1997) suggested that global modes in stellar disks can be coupled through non-linear interactions. They proposed that a wave 1 excites a wave 2 through second-order coupling terms that are large when CR of a wave 1 lies at approximately the same radius as the ILR of wave 2 (Sellwood 2013).

Many simulations of stellar disks show that the spiral arms fade out after some galactic rotations. Furthermore, if the effects of gas are not included, the velocity dispersion of the disk will increase; therefore the disk will become stable and will not form spiral arms (e.g. Sellwood & Carlberg 1984; Baba et al. 2009; Wada et al. 2011). Sellwood & Carlberg (1984) noticed that the spiral pattern in N-body simulations generally fades over time because the spiral arm structure heats out the disk kinematically and causes Toomre Q parameter to rise. Hence the disk becomes quite stable against the development of non-axisymmetric structures. It is also shown that the increment of new particles with low-velocity dispersion at a constant rate in the disk maintains the spiral patterns for longer time scales. Baba et al. (2009) performed self-consistent high-resolution, N-body+hydrodynamical simulations to explore how the spiral arms are formed and maintained. They also showed that spiral arms are not quasi-stationary, but they are transient and recurrent like alternative theories of spiral structures suggest (e.g. Goldreich & Lynden-Bell 1965; Julian & Toomre 1966; Toomre 1981).

Fujii et al. (2011) performed a series of high-resolution 3D N-body simulations of pure stellar disks. Their models are based on those of Baba et al. (2009) being the Toomre's Q initial parameter approximately one. They showed that stellar disks can maintain spiral features for several tens of rotations without the help of cooling. They also found that if the number of particles is sufficiently huge, e.g., larger than 3×10^6 , multi-arm spirals will develop on an isolated disk and they can survive for more than 10 Gigayears.

Baba et al. (2013) discussed the growth of spirals structures using one very high-resolution N-body simulation (3×10^8 particles). They pointed out that radial migration of stars around spiral arms are essential for damping of spiral structure because excessive Coriolis forces dominate the gravitational perturbation exerted by the spiral and, as a result, stars escape from the spirals and join a new spiral at a different position. This process is cyclic; therefore, the dominant spiral mode indeed change over radius and time.

Recent works made by Wada et al. (2011), Grand et al. (2012a), Roca-Fàbrega et al. (2013), Dobbs & Baba (2014) showed that the pattern speed of the spiral

arms decreases with radius similarly to the angular rotation velocity of the disc. Thus, the spiral arms are considered to be corotating with the rest of the disc at every radius; they are material spiral arms. In these models, the evolution of the spiral arms is governed by the winding of the arms, which leads to breaks and bifurcations of the spiral structure.

Other works have shown that the continuous infall of substructures from the dark matter halos of the galaxies could induce spiral patterns by generating localized disturbance that grows by swing amplification (Gauthier et al. 2006). However, D’Onghia et al. (2010) propose that dark matter substructures orbiting in the inner regions of the galaxies halos would be destroyed by dynamical processes such as disk shocking, moreover, hence would not be able to seed the formation of spiral structures. On the other hand, the interaction with galactic satellites could produce the growth of the spirals (Gerin et al. (1990), and references therein).

D’Onghia et al. (2013) developed high-resolution N-body simulations to follow the motions of stars. Firstly, they performed the simulation by using equal masses for each particle of the disk; then they added particles which have a similar mass of those of the molecular clouds. They demonstrated that eventually, the response of the disk can be highly non-linear and time variable. Ragged spiral structures can thus survive at least, in a statistical sense, long after the original perturbing influence has been removed.

Observational evidence in spiral galaxies supports both long and short-lived spiral patterns. Recently, based on the analysis with the Radial Tremaine – Weinberg method (Tremaine & Weinberg 1984) using CO and H_I data of several galaxies, it has been proposed that the spiral pattern speed Ω_p may increase with decreasing radius in some objects (Merrifield et al. 2006; Meidt et al. 2009; Speights & Westpfahl 2012). This behavior is also seen in simulations performed by Wada et al. (2011), Grand et al. (2012a), Grand et al. (2012b), Roca-Fàbrega et al. (2013). If this is indeed the case, the lifetime of the spiral structure is correspondingly very short. However, Martínez-García & González-Lópezlira (2013) use azimuthal age/color gradients across spiral arms to show that the spiral patterns in some grand design galaxies are long lived. Foyle et al. (2011) estimate that the torque produced by spiral patterns may redistribute the disk angular momentum in a time scale of approximately 4 Gigayears.

Recently, Saha & Elmegreen (2016) presented a series of simulations in which they changed the mass of the bulge. The models include the bulge which is a King model, an exponential disk, and a flattened, cored dark-matter halo. In some model with intermediate bulge mass, spirals structure have survived for several Gigayears. In their models, a “Q” barrier developed in those simulations are enough to avoid that the waves arrive at the ILR, and then, the wave can last for a long time.

In this work, we have generated a series of high-resolution N-body simulations ($\sim 10^6$ particles) in which we included halo, bulge, and disk components following the distribution functions described by Kuijken & Dubinski (1995).

The simulations were analyzed using 1D and 2D Fourier Transform methods. These analyses show the growth and evolution of spiral or bar structures. This paper is organized as follow. In Section 2, we describe the models and the FT1D and FT2D methods which are used to illustrate the growth of non-axisymmetric structures. In Section 3, we present the results of our analysis, the comparison with previous studies and a discussion. Finally, we summarize our findings in Section 4.

2. METHODOLOGY

2.1. *Setting up of the initial conditions*

We used the methodology delineated by Kuijken & Dubinski (1995) to generate the initial conditions of our models. In that work, they described methods for setting up self-consistent disc-bulge-halo galaxy models. Our models have been evolved from 0 to 5 Gigayears, with four free parameters: the disk radial velocity dispersion σ_R , the disk scale height z_d , the disk mass m_d , and the number of particles. Most of the structural parameters are given in table 1.

Figure 1 shows all the models that were evolved in this work. For all quantities, the reader can be referred to a normalization $UL = 3 \text{ kpc}$, $UT = 10^7 \text{ years}$, $UV = 293 \text{ km/sec}$, $UM = 6 \times 10^{10} M_\odot$, for $G = 1$. We have two sets of simulations: unbarred and barred models. The disk in unbarred models is stable against bar formation, but transient spiral structures can appear. On the other hand, the disk in barred models is unstable to bar formation, and it develops around the first gigayear in our simulations. The number of particles that we use in our models was of $N = 1.2 \times 10^6$ and $N = 8 \times 10^6$ particles. The higher resolution models are made in order to test the effect of interactions between disk particles with bulge and halo particles showing that the two-body relaxation will not artificially induce chaotic orbits, which could scatter particles out of resonant orbits. Also, we run some simulations in which the mass of the particles is the same for all the components. We resume these parameters in Table 2.

All our models generate similar rotation curves except for those models have the highest mass in the disk. As an example, Figure 2 shows the rotation curve resulted by model s27_z10D, and the initial Toomre stability parameter Q as a function of radius generated by the first 16 models listed on Table 2. The models with low values of Q will be called cold models. On the other hand, the models with high values of Q will be called hot models. We will discuss the evolution of the Q parameter in section 3.3.

2.2. *Temporal evolution of the models*

The simulations performed in this work employ the N-body code `gyrfalcON`, based on Dehnen (2000, 2002) force solver `falcON` (force algorithm with complexity) and the NEMO package (Teuben 1995). As tree-codes, `falcON` begins

$\sigma_{R,0}=0.27$ $z_d=0.20$ s27_z20D	$\sigma_{R,0}=0.37$ $z_d=0.20$ s37_z20D	$\sigma_{R,0}=0.47$ $z_d=0.20$ s47_z20D	$\sigma_{R,0}=0.57$ $z_d=0.20$ s57_z20D
$\sigma_{R,0}=0.27$ $z_d=0.15$ s27_z15X s27_z15D	$\sigma_{R,0}=0.37$ $z_d=0.15$ s37_z15X s37_z15D	$\sigma_{R,0}=0.47$ $z_d=0.15$ s47_z15D	$\sigma_{R,0}=0.57$ $z_d=0.15$ s57_z15D
$\sigma_{R,0}=0.27$ $z_d=0.10$ s27_z10X s27_z10D	$\sigma_{R,0}=0.37$ $z_d=0.10$ $M_d=1.47$ s37_z10M s37_z10X s37_z10D	$\sigma_{R,0}=0.47$ $z_d=0.10$ MW-A s47_z10D	$\sigma_{R,0}=0.57$ $z_d=0.10$ s57_z10D
$\sigma_{R,0}=0.27$ $z_d=0.05$ s27_z05X s27_z05D	$\sigma_{R,0}=0.37$ $z_d=0.05$ s37_z05X s37_z05D	$\sigma_{R,0}=0.47$ $z_d=0.05$ s47_z05D	$\sigma_{R,0}=0.57$ $z_d=0.05$ s57_z05D

Fig. 1. This Figure shows a grid of all our 26 simulations. The names of the models are at the bottom left corner. The models have different disk central radial velocity dispersions $\sigma_{R,0}$ and disk scale height z_d . These values are given in the upper right corner of each panel. The other parameters for the models are given in Table 1. The 16 black boxes correspond to models runned 1.2 million particles. The blue box represents the MW-A model (Kuijken & Dubinski 1995). The red box shows the models runned also with 8 million particles. The model in green box was also runned with different number of particles and different disk mass (see table 1).

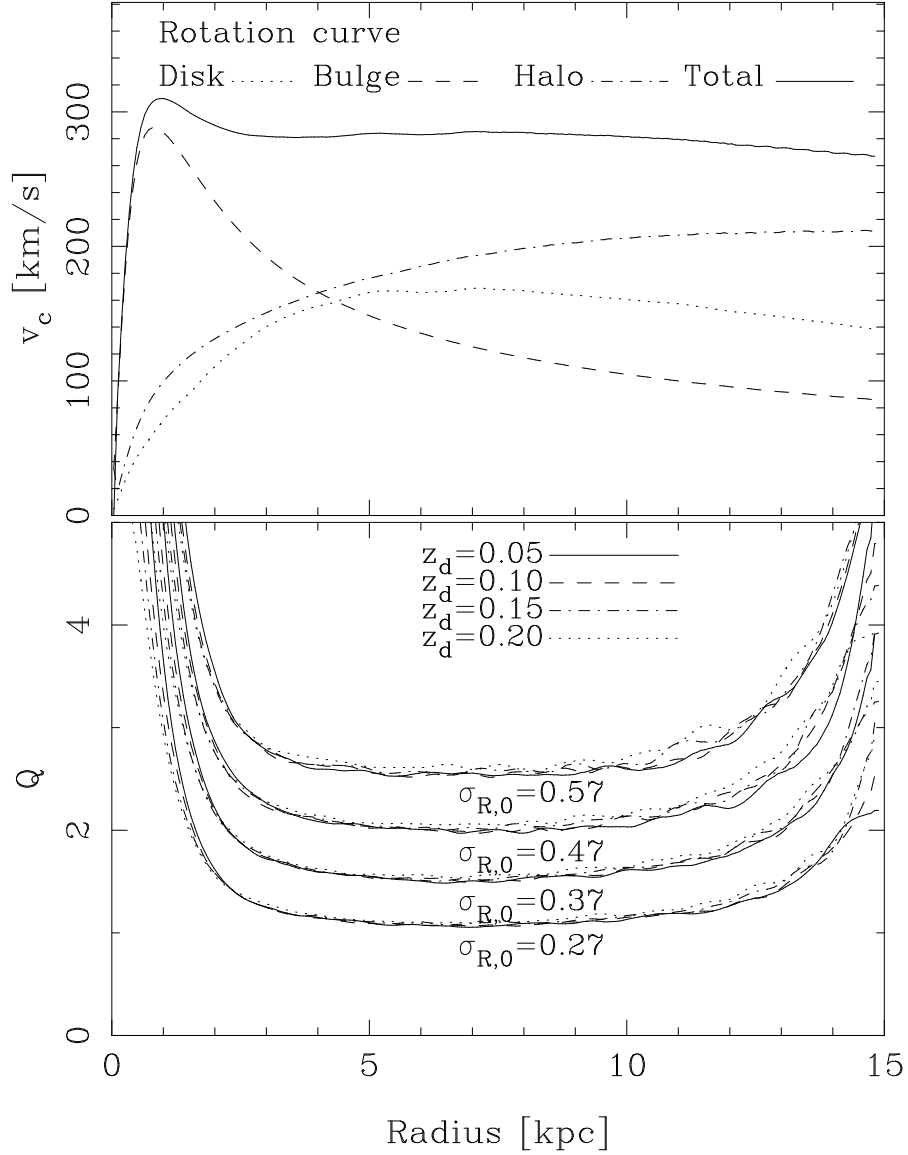


Fig. 2. Upper panel: the rotation curve generated by model s27_z10D. All our models have similar rotation curves, except the more massive disk one (barred models). Bottom panel: initial Q value for the 16 unbarred models with 1.2 million particles.

TABLE 1
MODEL PARAMETERS FOR THE MW-A MODEL.

Disk ^a				Bulge ^b				Halo ^c							
M_d	R_d	R_t	z_d	δR_{out}	$\sigma_{R,0}$	M_b	Ψ_c	σ_b	ρ_b	M_h	Ψ_0	σ_0	q	C	R_a
0.87	1.0	5.0	0.10	0.5	0.47	0.42	-2.3	0.71	14.5	5.2	-4.6	1.00	1.0	0.1	0.8

^a disk mass M_d , disk scale radius R_d , disk truncation radius R_t , z_d disk scale height, δR_{out} disk truncation width, disk central radial velocity dispersion, $\sigma_{R,0}$.

^b bulge mass M_b , bulge cutoff potential Ψ_c , bulge velocity dispersion σ_b , bulge central density ρ_b .

^c halo mass M_h , halo central potential Ψ_0 , halo velocity dispersion σ_0 , halo potential flattening q , halo concentration $C = R_c^2/R_k^2$, characteristic halo radius R_a (Kuijken & Dubinski 1994).

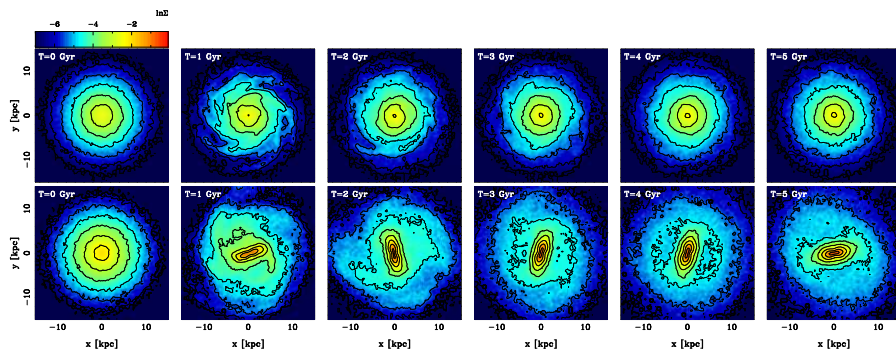


Fig. 3. Some snapshots of the models s27_z10D (top row) and s37_z10M (bottom row). The model with a light disk forms spiral structures which fade out after some rotations. The model with a heavier disk forms a bar, and this bar is maintained throughout the entire evolution. The time in Gigayears is given in the bottom left corner.

TABLE 2

THE TABLE SHOWS SOME PARAMETERS OF THE MODELS^a.

model	N_D	N_B	N_H	N_G	m_B/m_D	m_H/m_D	M_D/M_G	M_B/M_G	M_H/M_G	M_G
s27_z05D	320000	80000	800000	1200000	1.92	2.32	0.14	0.07	0.80	6.24
s27_z10D	320000	80000	800000	1200000	1.95	2.26	0.14	0.07	0.79	6.25
s27_z15D	320000	80000	800000	1200000	2.00	2.25	0.14	0.07	0.79	6.24
s27_z20D	320000	80000	800000	1200000	2.05	2.27	0.14	0.07	0.79	6.25
s37_z05D	320000	80000	800000	1200000	1.92	2.32	0.14	0.07	0.80	6.24
s37_z10D	320000	80000	800000	1200000	1.95	2.26	0.14	0.07	0.79	6.25
s37_z15D	320000	80000	800000	1200000	2.00	2.25	0.14	0.07	0.79	6.24
s37_z20D	320000	80000	800000	1200000	2.05	2.27	0.14	0.07	0.79	6.25
s47_z05D	320000	80000	800000	1200000	1.92	2.32	0.14	0.07	0.80	6.24
s47_z10D	320000	80000	800000	1200000	1.95	2.26	0.14	0.07	0.79	6.25
s47_z15D	320000	80000	800000	1200000	2.00	2.25	0.14	0.07	0.79	6.24
s47_z20D	320000	80000	800000	1200000	2.05	2.27	0.14	0.07	0.79	6.25
s57_z05D	320000	80000	800000	1200000	1.92	2.32	0.14	0.07	0.80	6.24
s57_z10D	320000	80000	800000	1200000	1.95	2.26	0.14	0.07	0.79	6.25
s57_z15D	320000	80000	800000	1200000	2.00	2.25	0.14	0.07	0.79	6.24
s57_z20D	320000	80000	800000	1200000	2.05	2.27	0.14	0.07	0.79	6.25
s27_z05X	2133333	533333	5333334	8000000	1.92	2.32	0.14	0.07	0.80	6.37
s27_z10X	2133333	533333	5333334	8000000	1.95	2.26	0.14	0.07	0.79	6.35
s27_z15X	2133333	533333	5333334	8000000	2.00	2.25	0.14	0.07	0.79	6.35
s37_z05X	2133333	533333	5333334	8000000	1.92	2.32	0.14	0.07	0.80	6.37
s37_z10X	2133333	533333	5333334	8000000	1.95	2.26	0.14	0.07	0.79	6.35
s37_z15X	2133333	533333	5333334	8000000	2.00	2.25	0.14	0.07	0.79	6.35
s37_z10M	320000	80000	800000	1200000	1.09	0.72	0.33	0.09	0.59	4.44
s37_z10MS	320000	87449	577113	984562	1.00	1.00	0.33	0.09	0.59	4.44
s37_z10MX	2133333	533333	5333334	8000000	1.09	0.72	0.33	0.09	0.58	4.40
s37_z10MXS	2133333	586831	3775591	6495755	1.00	1.01	0.32	0.09	0.59	4.48

The first column is the name of the model which indicates some initial conditions ($\sigma_{R,0}$ and z_d , see Figure 1). The number of particles of each component are given in columns 2 to 4, and column 5 shows the total number of particles for the system. Column 6 gives the mass ratio between bulge and disk particles, while column 7 gives the mass ratio between halo and disk particles. Columns 8 to 10 give the total mass ratios of the components. Finally, column 11 gives the total mass of the model M_G .

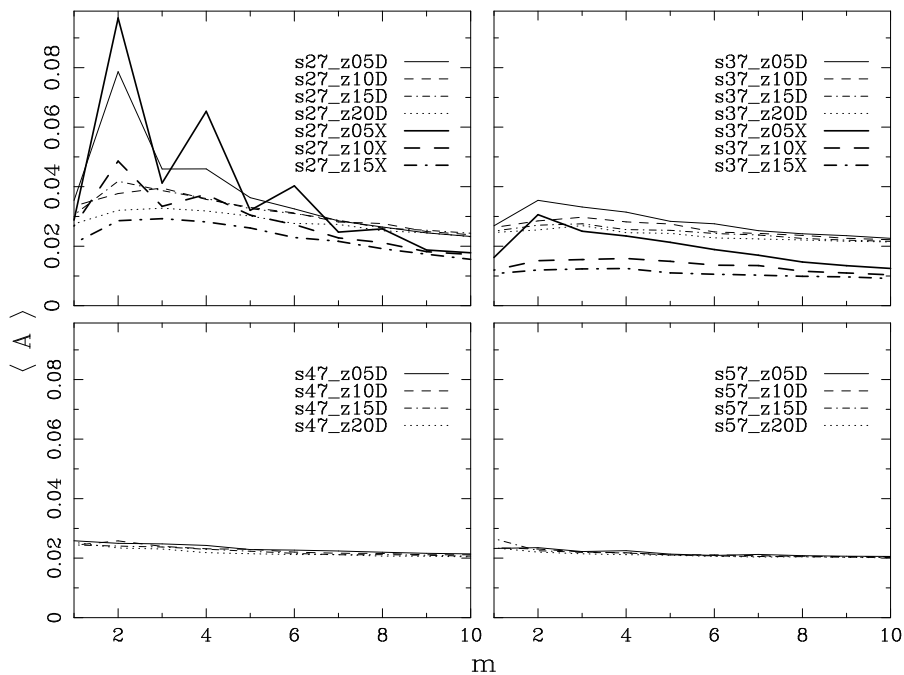


Fig. 4. The average amplitude $\langle A \rangle$ for modes m 1 to 10 for all unbarred models. The upper left panel shows the models with the lowest velocity dispersion (cold models) and the bottom right panel shows models with the highest velocity dispersion (hot models). While the coldest models generate strongest structures at mode $m = 2$, $m = 3$ and $m = 4$, which is evidence multi-armed structures, the hottest models do not generate structures.

by building a tree of cells at each time-step, then determines the potential of the system using multipole expansion for the cells and finally, exploits the similarity of the force from a distance cell upon cells that are close to each other.

In all our simulations, we used a softening parameter $\varepsilon = 0.05$ and an opening angle $\theta = 0.5$. With these parameters, we ensure that the energy conservation is better than 10^{-4} . The models were evolved from 0 to 5 Giga-years. Figure 3 shows six snapshots for models s27_z10D (top row) and s37_z10M (bottom row). The s27_z10D model forms transient spiral structures that fade out after some rotations, and the s37_z10M model forms a bar structure that is maintained throughout the entire evolution.

2.3. Analysis of Models

We studied the time evolution of the models using one and two dimensional Fourier Transform (FT1D and FT2D, respectively). High amplitude in the FT1D allows us to identify the region of disk where the perturbation is strong and the FT2D allows to get the pitch angle of the spiral structures. Thus, performing FT1D and FT2D over each snapshot allows showing how these

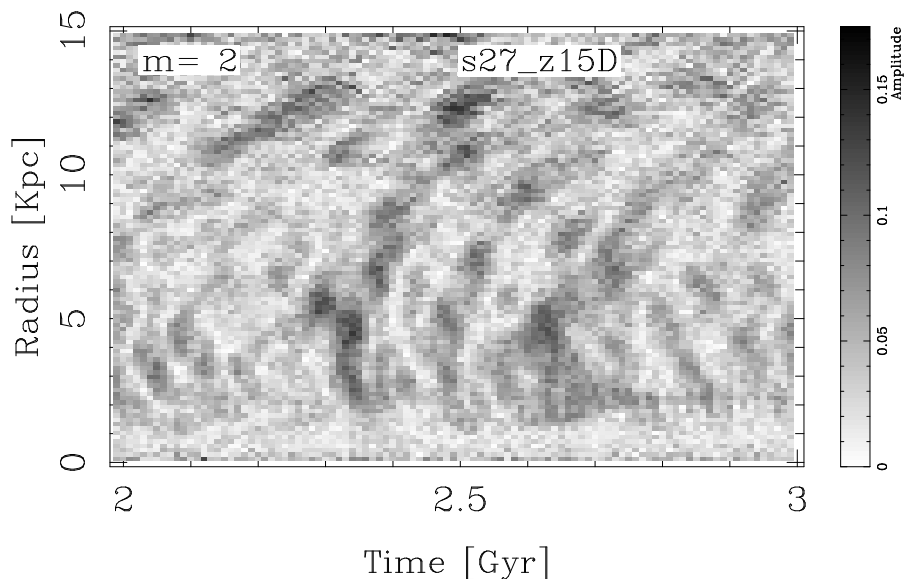


Fig. 5. Zoom of the FT1D for model s27_z15D for $m = 2$ as a function of radius and time. We can notice that the structures appear where the Toomre parameter Q is minimum (see Figure 2).

modes (the structures) and their pitch angles evolve during the simulation. Moreover, the phase of the FT1D coefficients gives information about the pattern speed of the structures (bar and spirals). We use the bar pattern speed to study the orbits of the particles in the bar reference frame.

In order to implement the FT1D, we divided the disk into 100 rings for each given time t (snapshot). Then, the FT1D is performed for each ring ($R = 1$ to 100) as follows:

$$A_R(m) = \frac{1}{D} \sum_{j=1}^{N_R} d_j e^{-im\theta_j} \quad (1)$$

where $D = \sum_{j=1}^{N_R} d_j$, θ_j is the azimuthal position of the j -th particle, N_R is the number of particles for a given ring, d_j is the weight of the j -th particle (in this case, we use the mass of each particle), and m is the azimuthal frequency. We use this equation to get the Fourier coefficients for each mode m and for each ring at each time step.

The FT2D method is applied to the distribution of the disk particles as described in Puerari & Dottori (1992) and references therein. We applied the FT2D in an annulus with a minimum radius equal to 4.5 kpc and a maximum radius of 15 kpc. The FT2D method is implemented by using a logarithmic spiral basis, $r = r_0 \exp\left(-\frac{m}{p}\theta\right)$; where m is a number of arms, and p is related to the pitch angle P of the spiral structure by $\tan P = -m/p$. The discrete FT2D is given by the equation:

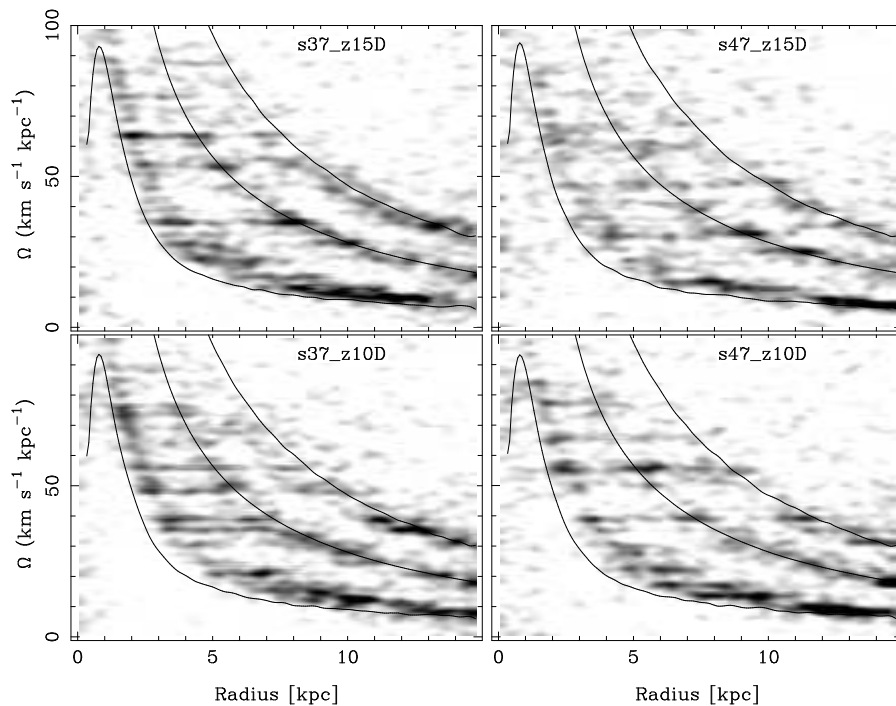


Fig. 6. Spectrograms given the pattern speeds of the structures for some unbarred models with 1.2M particles for the $m = 2$ mode. The curves are $\Omega + \kappa/2$, Ω and $\Omega - \kappa/2$. We note that the pattern speeds of the structures (dark regions) are well confined between the inner and the outer Lindblad resonances.

$$A(p, m) = \frac{1}{D} \sum_{j=1}^{N_A} d_j e^{-i(pu_j + m\theta_j)} \quad (2)$$

Here, $D = \sum_{j=1}^{N_A} d_j$, N_A is number of particles in the annulus, d_j is the weight of the j -th particle, $u_j = \ln r_j$, r_j and θ_j are the polar coordinates of the j -th particle. Thus, we applied the FT2D at each time step in order to obtain values of amplitudes $A(p, m)$ for each p and m . These results allow us to analyze the growth of the spiral structures and the evolution of their pitch angles.

3. RESULTS AND DISCUSSION

3.1. Unbarred models

In this section, we will present the calculations of the Fourier Transform methods (FT1D and FT2D); for the models with 1.2 and 8 million particles which do not form a bar.

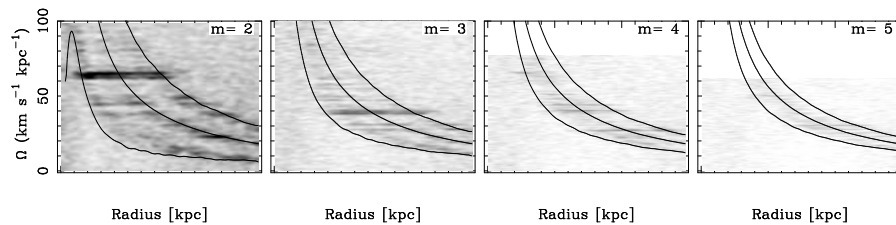


Fig. 7. Pattern speeds for the model s27_z15D for different m modes. The curves are Ω and $\Omega \pm \kappa/m$ corresponding to the main resonances. Dark regions correspond to the pattern speed of the structures. It is clear that this model develops multi-armed spiral structure. The pattern speeds of the structures for all m are well located between their main resonances.

3.1.1. FT1D for unbarred models

We summarize the results of FT1D amplitude for all unbarred models in Figure 4. The mean amplitude of a given mode m for each model was computed for all times and radii. In this Figure, the upper left panel shows the cold models, while the bottom right panel shows the hot ones. We have found that the cold models get the strongest structures at mode $m = 2$, and there are also some strong structures at modes $m = 3$ and $m = 4$; in fact, models s27_z05D and s27_z05X have a predominant mode at $m = 2$, due to the later formation of an inner oval and spirals. We conclude that the cold models are able to develop multi-armed structures, i.e. spiral structures with different azimuthal frequency number ($m = 2, m = 3, m = 4$), while it is clear that the hot models are unable to develop strong spiral structures with any azimuthal frequency.

In order to recognize where and when a m mode is amplified, we plot the Fourier coefficients $A_R(m)$ in gray-scale as a function of radius and time. The Figure 5 is an example of these plots. This plot shows the amplitude of the FT1D for $m = 2$ between 2 to 3 Gigayears for the s27_z15D model. The regions that have higher amplitudes (black stains) depict the growth of the structures. Especially in this graph, we can notice the evolution of a $m = 2$ structure appearing around a radial distance of 5 – 6 kpc. It worth to note that at those distances the Toomre parameter Q is minimal. From there, the higher amplitudes move towards the inner and the outer parts of the disk.

All our unbarred models follow this behavior. Furthermore, we can notice that the perturbation begins to be amplified where the stability criterion is minimum around 5 – 6 kpc (see Figure 2). It is known that models with low values of the Toomre parameter ($1 < Q < 1.2$), corresponding to cold models (Binney & Tremaine 1987), have the capability to develop non-axisymmetric structures via swing amplification while models with high values of the Toomre parameter ($Q > 2$), corresponding to hot models, are unable to form structures in the linear regime. Indeed, our cold models (lower Q) are able to amplify strong non-axisymmetric structures (Figure 4).

Our next step is to measure the location and the pattern speed of the

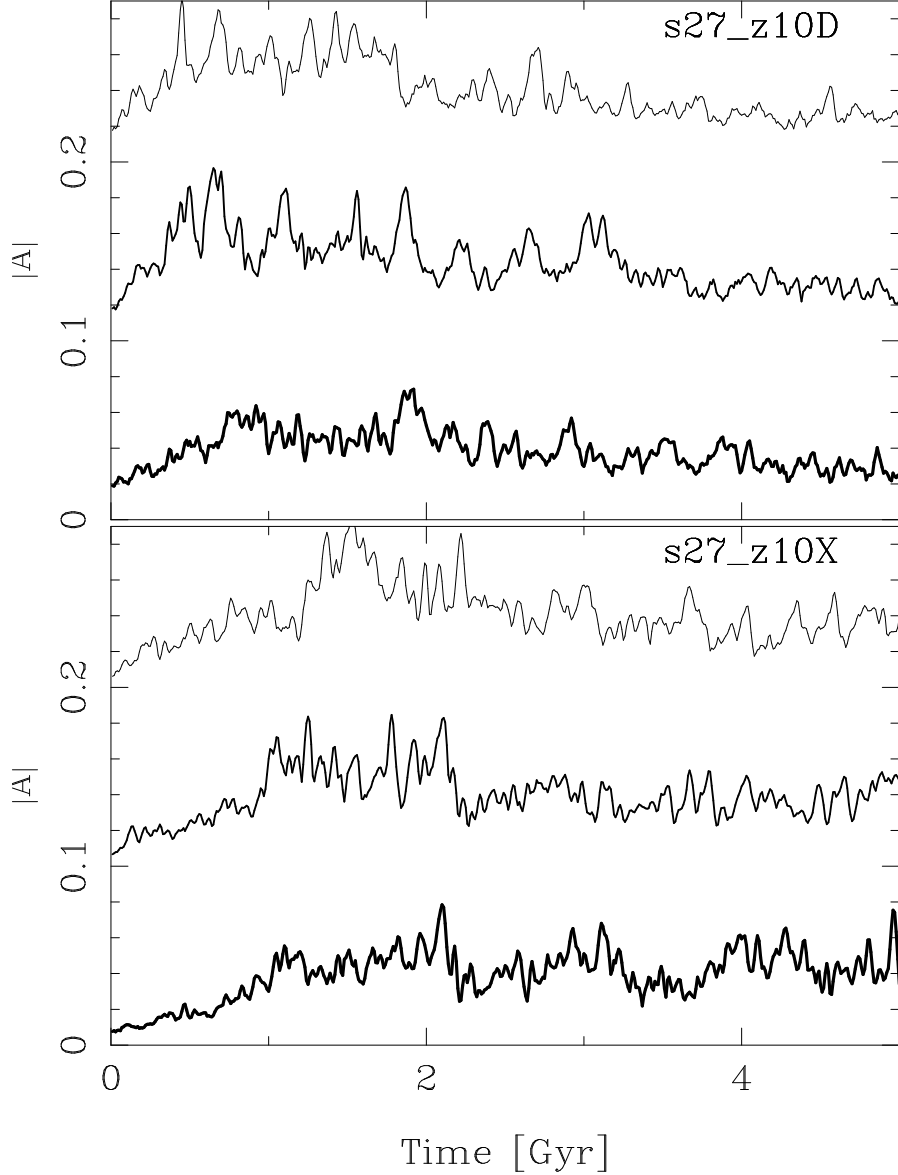


Fig. 8. These plots show the average amplitude $|A|$ for mode $m = 2$, $m = 3$, and $m = 4$. We add 0.1 and 0.2 to the $m = 3$ and $m = 4$ for clarity. The mean was calculated in the radial range 3.75 to 12.75 kpc. The thickest line is for mode $m = 2$, the intermediate thick line is for mode $m = 3$, and the thinnest line is for mode $m = 4$. The upper panel shows the amplitudes for the model with 1.2 million particles, and the bottom panel shows the amplitudes for the model with 8 million particles. We can see that these models generate multi-armed structures. Furthermore, we observe that the model with low mass resolution generates structures earlier than the model with high mass resolution.

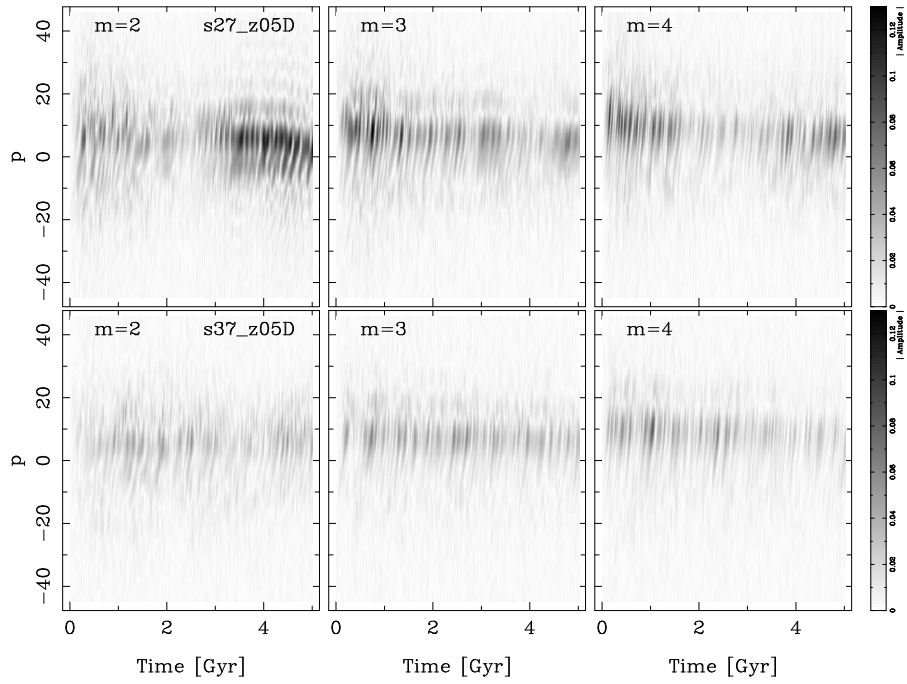


Fig. 9. The amplitudes of the FT2D for $m = 2$ for two of our unbarred models. Leading structures correspond to $p < 0$, and trailing ones correspond to $p > 0$. We can see how the amplitudes oscillated with time; these oscillations are due to the superposition of waves with different pattern speeds.

structures. Figure 6 shows spectrograms of the $m = 2$ perturbations as a function of radius for the entire evolution of these bisymmetric structures for four of our models. The darker areas correspond to the angular velocity of the strongest structures that are evolving in the disk. We can note that these structures are constrained to be located between the ILR and the OLR resonances implying that there are different structures with different pattern speed in the same radius. Additionally, Figure 7 shows the pattern speeds of the s27_z15D model for different modes m modes illustrating that structures with different m 's can co-exist in the galactic disk. Like in Sellwood (2011), Sellwood & Carlberg (2014), Valencia-Enríquez & Puerari (2014) and Mata-Chávez et al. (2014), these Figures suggest that a spiral structure is the result of the coupling of structures of a m mode and different pattern speeds, but also they are coupling in different parts of the disk. The general morphology of our modeled galaxies is due then to the superposition of several different modes.

We also have evolved some models with larger number of particles to investigate the growth of the spirals. In this case, we calculated models with 8 million particles (see Figure 1), i.e., we increased the number of particles by a factor of 6.6. Figure 8 shows the amplitude of the FT1D for different modes m as a function of time. The upper panel shows the amplitude for the s27_z10D model (model with 1.2 million particles), and the bottom panel shows the amplitude for the s27_z10X model (same model with 8 million particles). These two panels are similar; this implies that the behavior of the model with more resolution is akin to the model with less resolution.

Therefore, all unbarred models (with both higher and lower resolution) have similar behavior as we described before. However, the structures formed in these higher mass resolutions runs appeared a bit later and are weaker than the structures formed in the less mass resolution runs. It means that the heating of the disk for higher resolution models is weaker than the heating of the disk for lower resolution models. The heating is due mainly to spiral activity and collisional relaxation. The collisional relaxation is a minor effect compared to the physically real collective heating caused by spirals. Hence, the high-resolution models have less heating because the spirals are weaker.

Fujii et al. (2011), Sellwood (2013) and Sellwood & Carlberg (2014) explored models with a different number of particles N in the disk. Fujii et al. (2011) found that the two-body relaxation has effects on the heating of the disk only when the number of particles is quite small, while Sellwood & Carlberg (2014) explained that the spiral activity causes the heating of the disk and the two-body relaxation is controlled by the softening in the force computation.

We must note that our models with a high and low number of particles have the same softening. The high-resolution models heat a bit later because the two-body relaxation is less important than those with low resolution. The spiral activity on high-resolution disk makes less heat than low-resolution disk due to the smaller amplitudes of the perturbations. We will strength this statement in section 3.3 where we discuss the evolution of the Q parameter

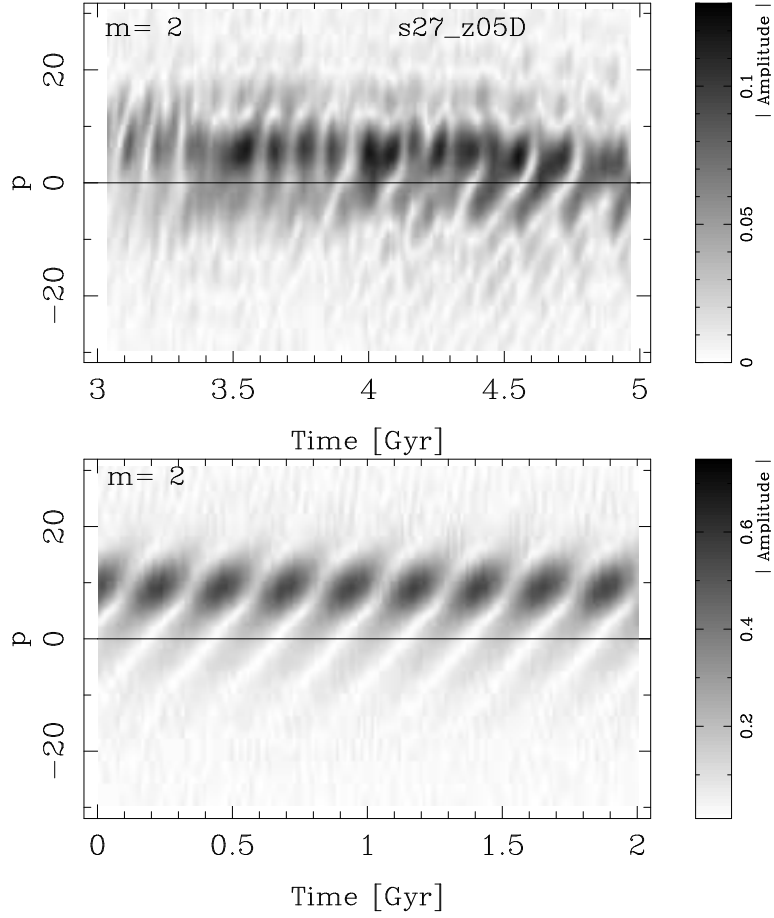


Fig. 10. Upper panel: Zoom of FT2D at $m = 2$ amplitudes for s27_z05D model. Spiral structures with different pattern speeds ‘beat’ as waves to give these appearance of periodicity in the amplitudes. Bottom panel: The FT2D calculated using two spirals with different pitch angles and angular speeds. The superposition of these two spirals gives a Fourier Transform coefficients behavior very similar to that one of ours modelled galaxies.

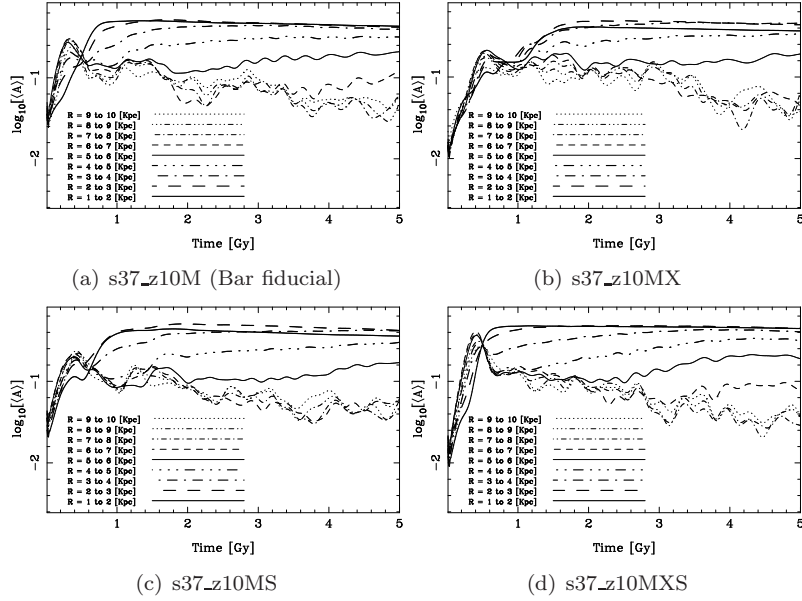


Fig. 11. The average of the FT1D amplitude for some radial ranges for the massive disk models for $m = 2$. In these plots, one can note as the amplitude for inner radii grows and becomes more or less constant, representing the formation of the bar in the disk. The amplitude for outer radii oscillates representing the formation of transient spiral structures.

for all models.

3.1.2. *TF2D for unbarred models*

We performed the FT2D on all our models, but for simplicity, we only present in Figure 9 the results for two of our models for modes $m = 2$, $m = 3$, and $m = 4$. In this Figure, each panel depicts the Fourier coefficient (the amplitude) $|A(p, m)|$ on gray-scale as a function of time, and frequency p . (see Section 2.3). In these charts, the highest amplitudes represents the spiral structures which are appearing in the disk, and the black stains shows the evolution of these structures.

The oscillations we can see in the amplitudes of the spiral patterns are a signature of superposition of structures – or modes – with different values of pitch angle and angular speeds. Such modes were already detected using the FT1D spectrograms (see e.g., Figures 6 and 7).

In the upper panel of Figure 10, we present a zoom of the FT2D amplitude for mode $m = 2$ between three and five Gigayears for the s27_z05D model, which is the coldest and thinnest model. In the bottom panel, we show a FT2D calculation where we simulated 2 different spirals with pitch angles 14 and 12.5 degrees. One spiral rotates with an angular speed of 48 km/sec/kpc, while the other one rotates with $\Omega = 35$ km/sec/kpc. The superposition of these two spirals gives a FT2D very similar to those we are measuring in our

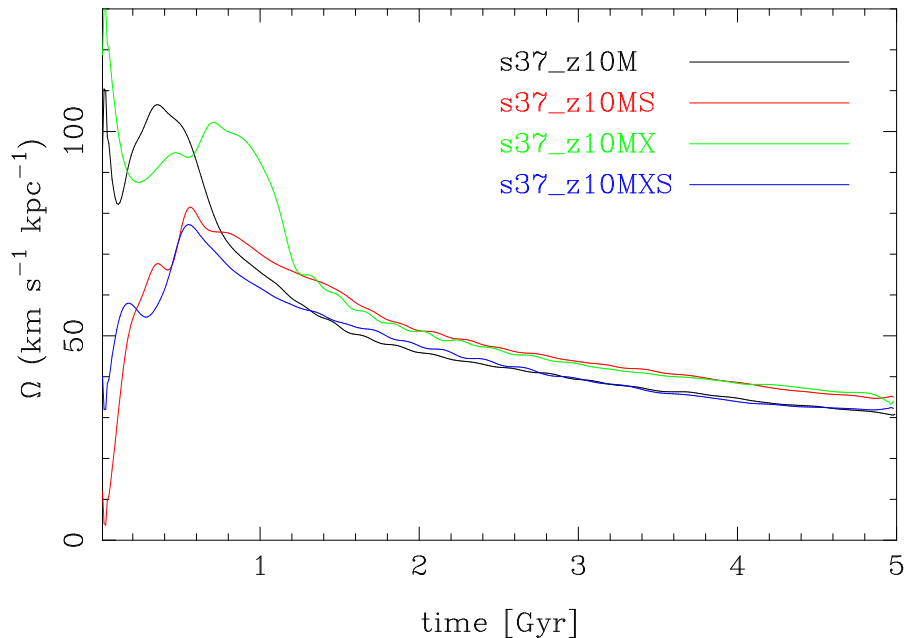


Fig. 12. This Figure shows the pattern speed of the bar as a function of time during the entire evolution for all barred models. The angular speed decreases in all models, from approximately 70 – 80 km/sec/kpc at the first Gigayear to 30 – 35 km/sec/kpc at end of our calculations, at 5 Gigayears.

simulations. Then, once again we emphasized that the Fourier analysis is showing that the general morphology of our modeled galaxies is due to the superposition of several different modes.

All our models, including models with high and low mass resolution, follow this behavior that was explained before. Moreover, we remark that the coldest/thinnest models generate strong spiral structures, while the hottest/thickest models do not generate structures. On the other hand, Sellwood & Carlberg (1984) argued that the spiral arms in N-body simulations generally fade out over time because the spiral arms heat the disc kinematically and cause the Q to rise. Our models also show this behavior where the Q parameter is increased. We show the increment of Q in section 3.3.

3.2. Bar models

In this section, we will follow our analysis as we performed in section 3.1, but now on our barred models. For these models, we also present an orbital analysis in order to show the growth of the bar.

3.2.1. TF1D for barred models

In our sample of simulations, we ran models with a more massive disk (see Figure 1 and Table 2). These models clearly developed a bar feature because

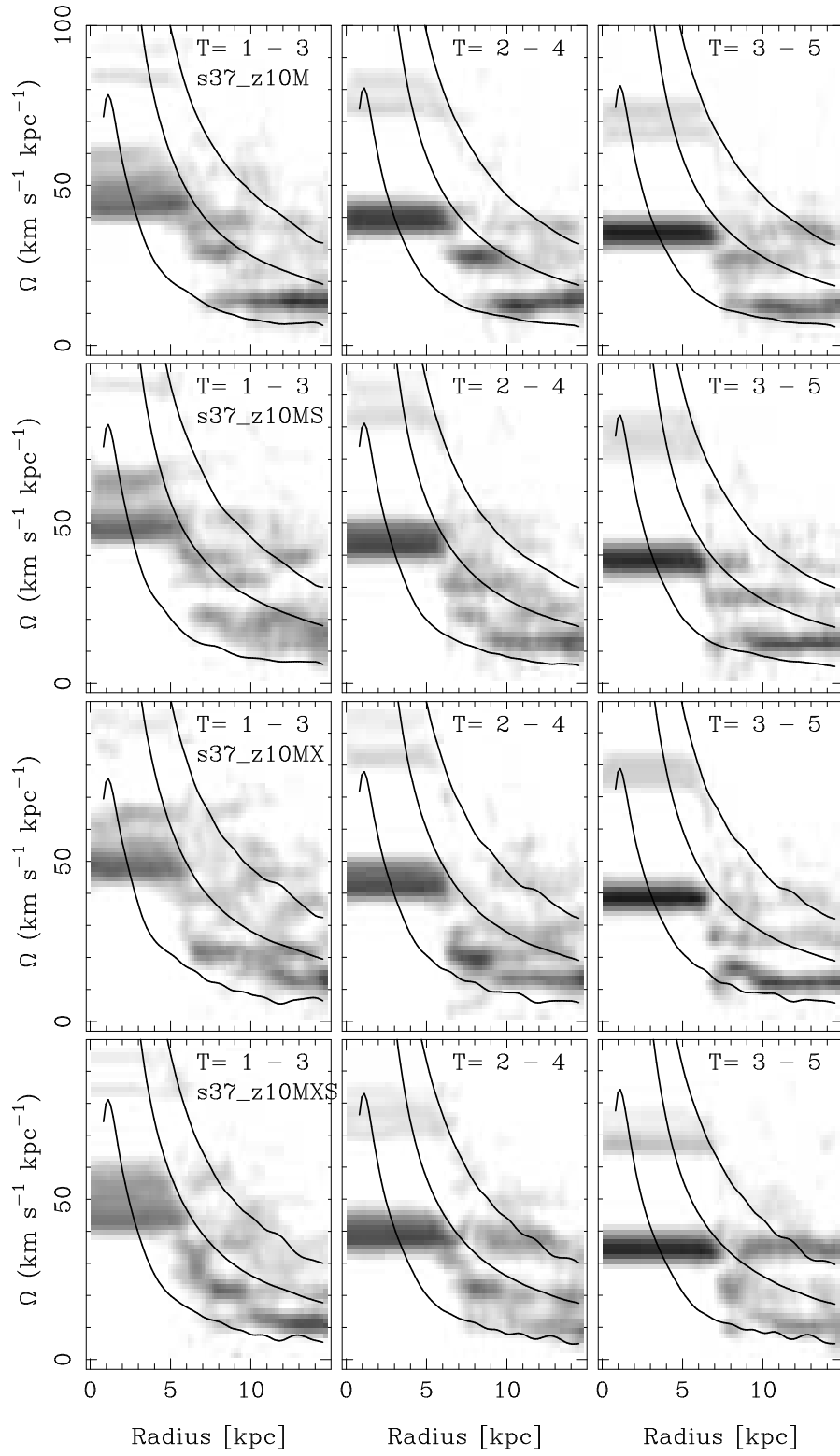


Fig. 13. This Figure shows the spectrograms which were calculated for three-time intervals. We can see how the bar slowdown in its evolution. It is also clear that the spirals rotate slower than the bar (see text).

they had a quite low initial Q value at the beginning of their evolution due to the higher disk surface density.

We applied the FT1D in the same way as in the previous models to analyze the growth of the bar and the spiral structures that are formed in the disk. The results of the FT1D are shown in Figure 11. Each panel of this Figure shows the mean amplitude $\langle A \rangle$ (equation 1) in logarithmic scale for $m = 2$ as a function of time and radius for each model. These plots can be understood as growing curves of the structures that are being assembled. We can observe that the evolution of the amplitude is akin between all barred models, the main difference being the bar's growing rate. For example, the amplitude in the inner disk between 1 – 2 kpc for model s37_z10M (called bar fiducial model) reach its maximum approximately at 0.9 Gyr of its evolution while for model s37_z10MX reach its maximum approximately at 1.4 Gyr. On the other hand, while the model s37_z10MS reach its maximum approximately at 1 Gyr, the model s37_z10MXS reach its maximum much earlier, at 0.6 Gyr.

In order to calculate the instantaneous bar pattern speed as a function of time, we calculate the angle θ of the bar from the phase ϕ of FT1D for $m = 2$ taking the mean value of θ in a radial range from 0.15 to 2.25 Kpc, getting then a $\theta(t)$ curve. We then fit a straight line each 5 points on the $\theta(t)$ curve and take its slope for the middle point as a result of pattern speed $\Omega_p(t)$. Figure 12 shows $\Omega_p(t)$ for all barred models. It depicts the evolution of their instantaneous bar pattern speed evidencing that the bars appear with high angular velocity, and they slow down throughout the time. Athanassoula (2014) showed that this decrease of the pattern speed could be explained as due to the angular momentum exchange within the galaxy or by the dynamical friction exerted by the halo on the bar. In a forthcoming article (Valencia-Enríquez et al., in preparation) we will present results focused in a large set of isolated/interacting barred galaxy simulations to get insight on the processes which speed up or slow down the bar.

In Figure 13, we present the $m = 2$ spectrograms of these simulations, now calculating them for three different time intervals (1 – 3, 2 – 4, 3 – 5 Gyr). This calculation allows us to compare the bar pattern speed and the spirals pattern speed. We can clearly observe the bar pattern speed in the inner part of the disk with high amplitude (dark horizontal line), and the pattern speed of the spirals in the outskirts of the disk with a bit less amplitude.

The spectrograms of all barred models in the Figure 13 show that the bar slows down more than the spiral. Furthermore, the bar rotates around twice as fast as the spiral structures. The spiral structure, as in the previous cases, results from the superposition of several $m = 2$ modes with different pattern speeds at different radial regions (see Minchev & Famaey 2010 for an extensive discussion on the spiral–bar resonance overlap). The difference between barred and unbarred models is that in barred models, there are more $m = 2$ modes being amplified, probably due to the influence of the strong fast rotating central bar.

Also, we show the main resonances curves to identify whether the bar has

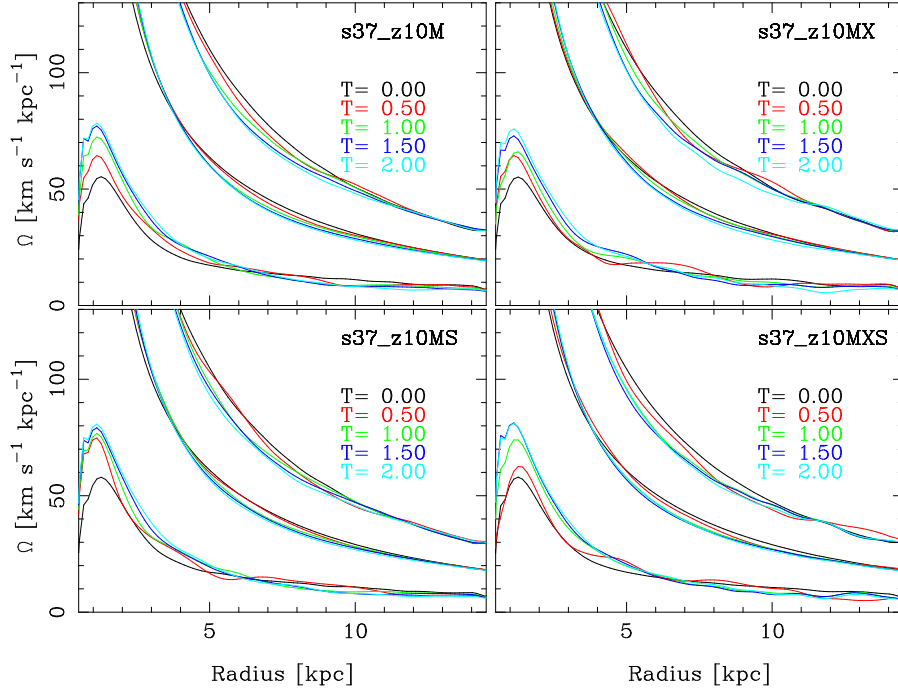


Fig. 14. This Figure shows angular frequency Ω (middle lines), $\Omega - \kappa/2$ (bottom lines), and $\Omega + \kappa/2$ (upper lines) at different times for all bar models.

an ILR. These results are shown in Figure 14. To get these curves, we obtain Ω from the circular velocity of the model, and the main resonances from the equations $\Omega \pm \kappa/2$ where κ is the epicycle frequency ($\kappa^2 = R \frac{d\Omega^2}{dR} + 4\Omega^2$). This Figure shows the Ω and the main resonance for all barred models from 0 to 2 Gigayears. We can observe that all our models have a high ILR in the inner region of the disk because of the presence of a strong bulge, and it is rising due to the increasing of the density in the center of the disk across their evolution. Yet, we must note that the bar appears with very high angular velocity (see Figure 12), higher than the top of the ILR at the beginning of the simulation (see the ILR in Figure 14 at $T = 0$ drawing with black line) implying the bar is probably formed in the linear regime (Athanassoula & Sellwood 1986), but after some time the bar slows down quickly and the top of the ILR overtakes the angular velocity of the bar. It happens probably due to the exchange of angular momentum (Athanassoula 2003 and references therein). The bar finally evolves having an ILR (Okamoto et al. 2015).

3.2.2. TF2D for barred models

For barred models which have a heavier disk (green box in Figure 1), the FT2D was separately computed for both bar ($0.1 < R < 4.5$ kpc), and disk ($4.5 < R < 15$ kpc) regions. Figure 15 shows the Fourier coefficients of FT2D for the fiducial model; the results of the FT2D for the other barred models

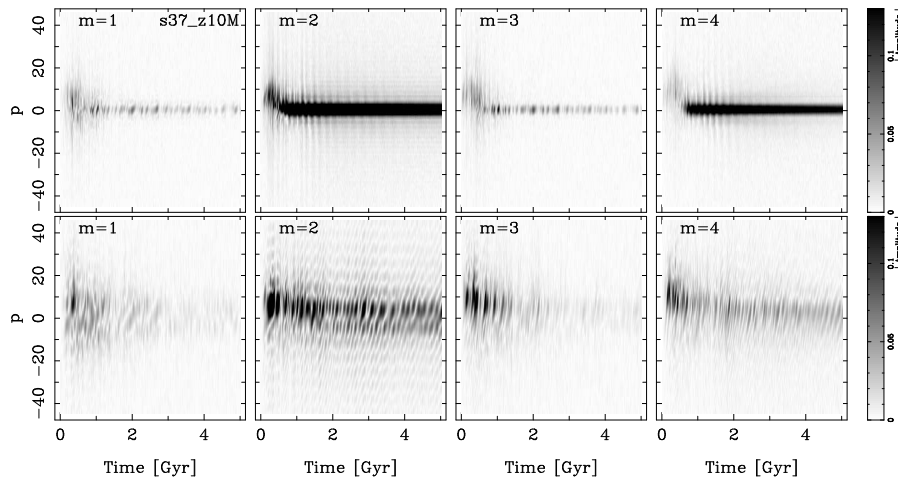


Fig. 15. Upper panels show the amplitude of the FT2D from $m = 1$ to $m = 4$ for the fiducial bar model. The FT2D was calculated at an inner radial region $0.1 < R < 4.5$ kpc. The maximum amplitude being found for the Fourier coefficient $A(p = 0, m = 2)$ is a clear sign of the presence of a bar. Bottom panels show the amplitude of the FT2D for the same modes m , but for the outer radial region $4.5 < R < 15$ kpc. In the barred cases, the spiral structures are stronger than in the unbarred ones. For the outer radial region, higher azimuthal frequencies are triggered at the time of the bar formation.

are very similar. The upper panels of this Figure clearly show the presence of a bar structure; there is very high amplitude for $m = 2$ and $p = 0$. The bottom panels show the spiral arms that are growing in the disk.

Similarly to section 3.1.2, we zoom of the $A(p, m = 2)$ coefficients in the interval between 3 and 4 Gigayears for the disk ($4.5 < R < 15$ kpc) region. These results are shown in Figure 16. In this Figure, we note that the spiral structures get stronger due to the presence of a bar (Buta et al. 2009) compared to the lighter disk simulation (see Figure 9), All in all, the spiral waves in this barred model have a similar behavior to the unbarred models. Which is a clear evidence of effects of the coupling of the spiral structures, now reinforced with the central bar.

3.2.3. Orbits for the barred models

We now focused our interest on an analysis of the disk stellar orbits in the bar reference frame. For example, Chatzopoulos et al. (2011) proposed a complete analysis of the stellar orbits in test particles of gravitational potentials which are based on tracing patterns in sequences of characters, which indicate sign changes of the Cartesian coordinates. On the contrary, we propose a very simple geometrical method in which we analyze three morphological types of orbits in the bar reference frame. For illustration, we show in Figure 17 the morphological evolution of six orbits for the fiducial barred model. We can clearly notice that a given particle is not confined to one only type

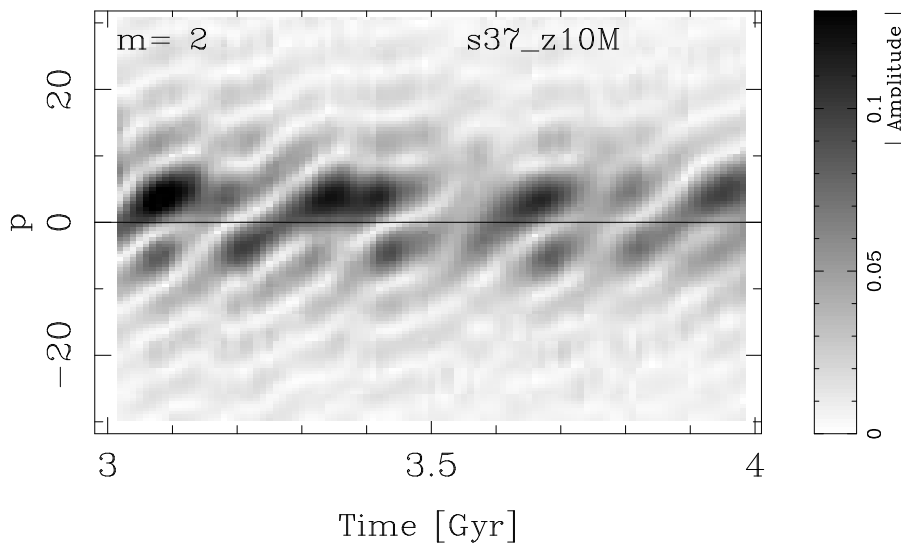


Fig. 16. Zoom of the FT2D amplitude at $m = 2$ mode for the barred model calculated in the radial interval $4.5 < R < 15$ kpc. We can observe that both leading ($p < 0$, with less amplitude) and trailing spiral structures ($p > 0$, with higher amplitude) appear for a given time due to the superposition of waves with different pitch angles and angular speeds. Besides, we can note the amplitude of these spirals is higher compared to those of the unbarred models (Figure 10).

of morphology; they change their morphologies during their entire evolution (Athanasoula 2012).

In order to make the analysis of the stellar orbits which evolved with the bar formation, we graphically classify the orbits of the disk particles in three primary morphological types as follow: orbits that are concentrated at the galactic center (compacts, C), orbits that are along the bar (bar, B), and orbits that are around the Lagrangian points L_4 and L_5 (loop orbits, L). We developed a code to choose these type of orbits where we take our bar reference frame in a vertical position, and we used the following criteria. The criterion to classify barred type orbits is $|y_{max}| > 1.9|x_{max}|$ where $|y_{max}|$ is the maximum position value of a given particle in the vertical component (along of the bar) and $|x_{max}|$ is the maximum position value of the same particle in the horizontal component (perpendicular to the bar). The criterion to classify compact type orbits is $r_{max} \leq 0.5$ kpc, where r is the maximum radius of a given particle. Finally, the criterion to classify loop type orbits is that the particle orbit is confined to one side of the bar. Particles not following either of our three criteria are then unclassified (NC). These criteria were used for all disk particles for each one Gigayear interval.

Furthermore, we have to keep in mind that the bar appears around 1.5 Gigayears for the s37_z10MX model, and around 1 Gigayear for other models. Hence we made this orbital analysis from T=1 to T=5 Gigayear for all barred models. These results are shown in Figure 18. This Figure shows the sta-

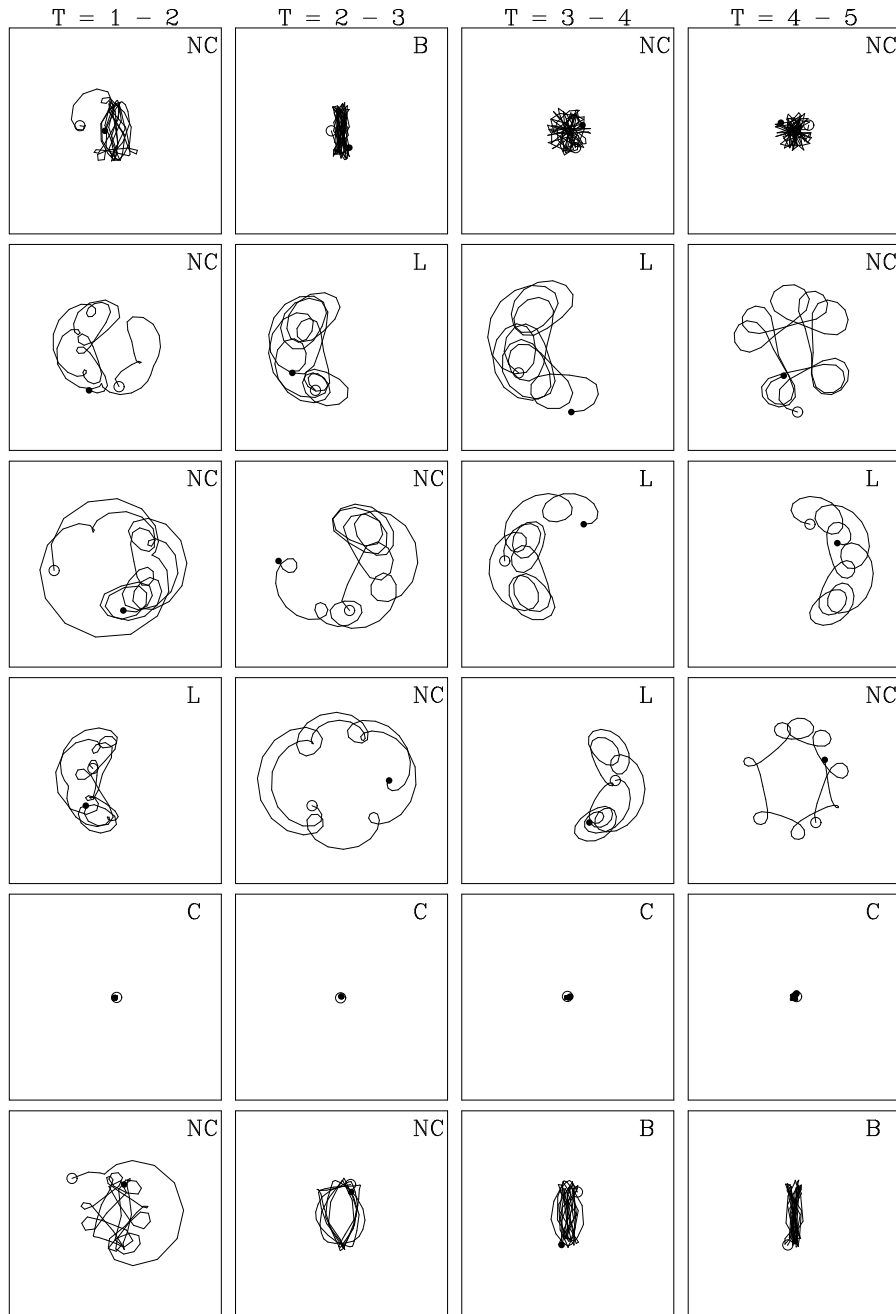


Fig. 17. Morphological evolution of six particles of the s37_z10M model. At each row, we plot the orbit of the same particle in 4 different time intervals. The orbit classification is given at the upper right corner. We can observe that a particle is confined to an orbit type morphology, but they can change during its entire evolution.

tistical classification of these three types of orbits which are weighted on the percentage of disk mass. We can see in this Figure that the general behavior is akin to the all barred models. For example, with the bar formation, the number of their compact orbits have a little growth, and their loop orbits have a more pronounced growth. The number of their bar orbits remains more or less constant after the second Gigayear.

These models have the same initial conditions; the only difference is the number of particles, which defines the mass of the particles. This difference makes that the noise affects a little bit different the evolution of the models (Sellwood 2003). For example, we can find that the model s37_z10MS has more compact orbits than the other models, the number of loop orbits is almost equal to the fiducial models, and this forms approximately 4% fewer bar orbits than the fiducial model. The largest model (s37_z10MX) keeps its compact orbits around 4% across its entire evolution, this model has 1.5% fewer loop orbits and 3% fewer bar orbits than the fiducial model afterward the second Gigayear. Finally, we can see that the another one large model s37_z10MXS is the most similar to the fiducial model because its differences in all type of orbits is around 1%.

In general, the compact type orbits increase their number up to 5% of the disk mass, the loop type orbits increase their number to achieved around 10% of the disk mass for all of the models, and the bar type orbits increase their number to attain around of 15%, 13%, 12% and 16%. for fiducial, s37_z10MX, s37_z10MS, and s37_z10MXS models, respectively. Finally, we have found that these three geometrically classified type of orbits, which are the ones trapped in the Lagrangian points L_3 , L_4 , and L_5 , encompass approximately one-third of the disk total mass for these bar models.

3.3. Toomre stability parameter Q

We already have discussed that the thickness of the disk z_d affects the formation of non-axisymmetric structures. For example, Figure 4 shows that the models with a very thin disk (e.g. s27_z05D or s27_z05X) form stronger structures than models with thicker disks demonstrating that the local instabilities of the disk also depends on its thickness.

It is already known that the stability of the disk is measured by the Toomre parameter Q in the standard first order perturbation where the disk is considered like a very thin, self-gravitating disk (Binney & Tremaine 1987; Bertin & Lin 1996). However, as we said before, the thickness of the disk is also related with the stability of the disk, and so it is convenient to study the stability of the disk (Q) for different values of the vertical scale height z_d .

The measure of the Q as a function of radius at three different times (0, 2.5, and 5 Gigayears) for unbarred models is shown in Figure 19 evidencing that the models with low/high velocity dispersion have low/high values of the parameter Q . Additionally, we note that the hotter models, in upper panels, keep the parameter Q approximately constant through the time while the initially colder models, in bottom panels, present an increment of Q .

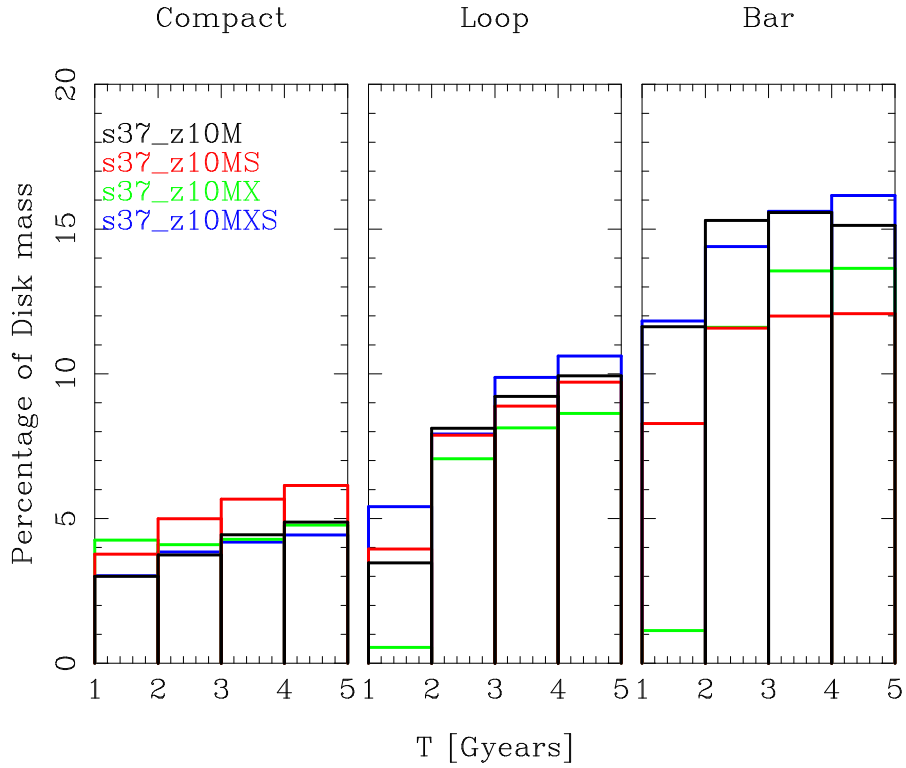


Fig. 18. Morphological classification for all disk particles orbits at 4 times intervals. The left panel shows the compact type orbits, the middle panel shows loop type orbits, and the right panel shows bar type orbits. At the end of our calculations (5 Gigayears) these three type of orbits enclosed approximately one-third of the disk mass (see text).

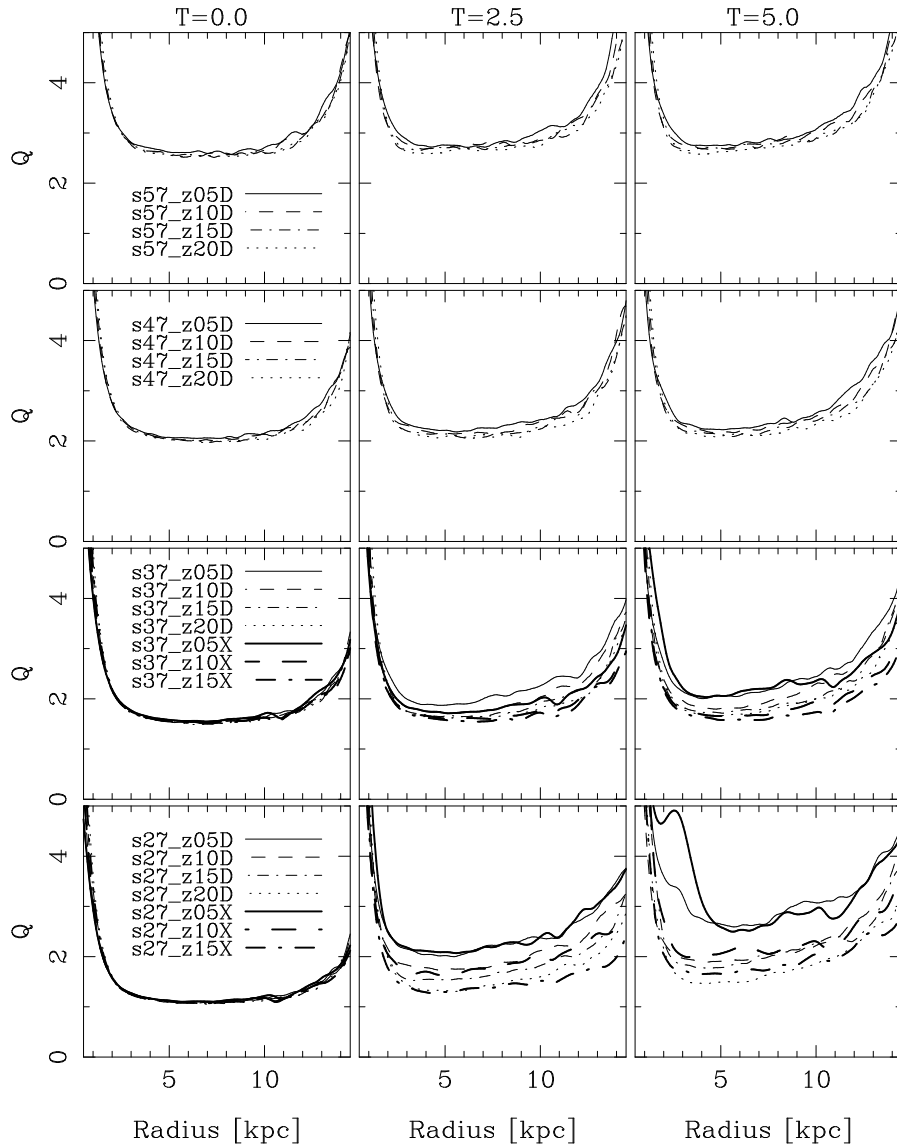


Fig. 19. The evolution of the Q parameter as a function of radius for all unbarred models. The Q parameter is shown at $T=0$, 2.5, and 5 Gigayears (see text).

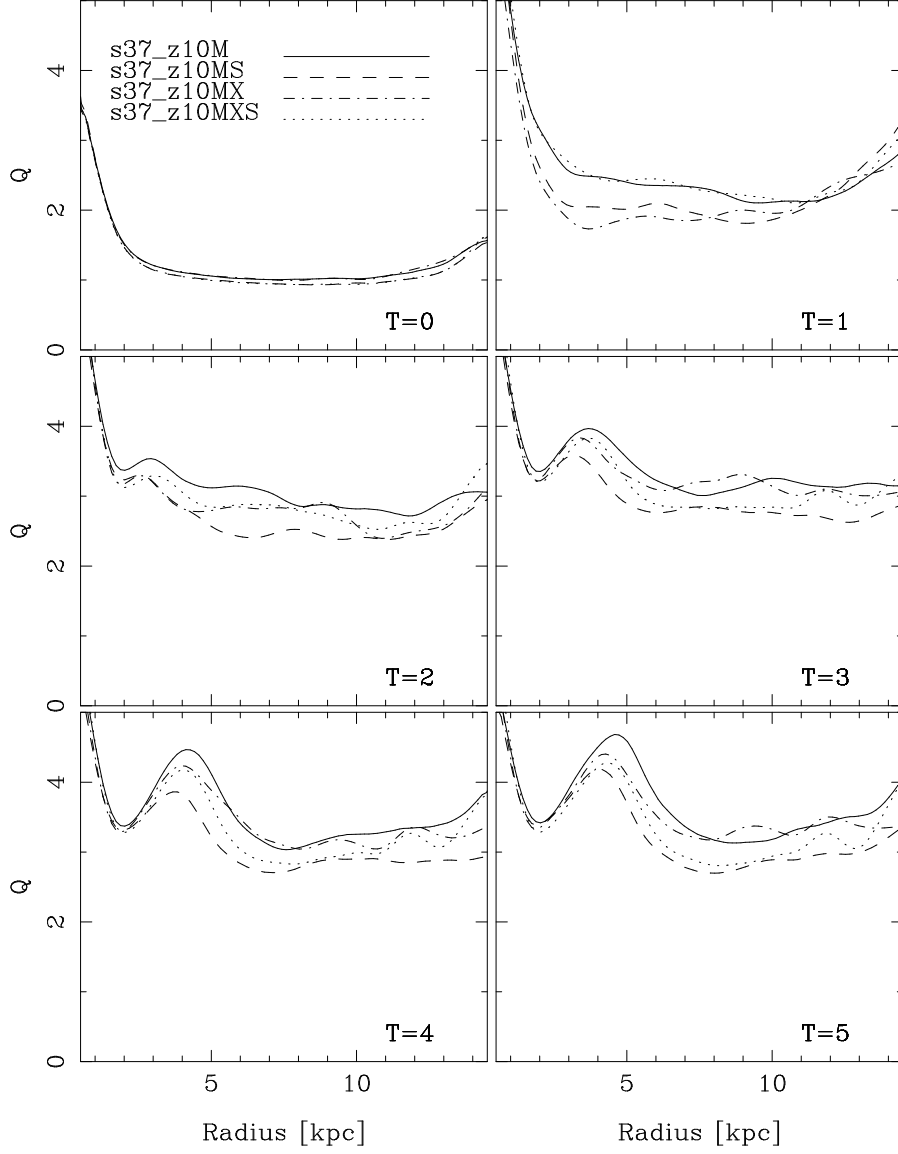


Fig. 20. The Figure shows the evolution of the Q parameter as a function of radius for the barred models. The Q parameter for all barred models have low values at the beginning of the simulation, but it increases considerably due to the bar and spirals formation.

Furthermore, it depends strongly on the initial disk thickness z_d . For example, the increment of Q for model s27_z05D (or s27_z05X) is more conspicuous than the increment of Q for model s27_z20D which has a thicker disk. Hence, the stability of the disk should depend on the velocity dispersion in the z component (σ_z), the vertical scale height z_d , and mass of the disk. These results have also been discussed in Klypin et al. (2009).

We also measure the evolution of Q parameter for barred models; these results are shown in Figure 20. We can see in this Figure that the parameter Q is lower at the beginning of the simulation, but it increases quickly due to the bar and spiral formation. However, as the bar reaches its saturation and evolves far from the linear regime, the increment of Q does not affect the bar strongly evolution and neither the maintenance of the spiral structures.

Additionally, we have to claim that the models with few and high number of particles and same initial conditions heat the disk in similar way (see Figures 19, and 20). Sellwood & Carlberg (2014) explain that this behavior is due more to the spiral activity than to the two-body relaxation (Fujii et al. 2011). Moreover, it also depends on the softening parameter, if this is quite small, then the two body-relaxation could be important in the evolution of the model (Sellwood 2013), and the disk is quickly heating. See also (Romeo 1998) for an extensive study on the softening choice.

4. SUMMARY AND CONCLUSIONS

We performed a series of 3D fully self-consistent N-body simulations with 1.2 and 8 million particles. The initial conditions were chosen to follow Kuijken-Dubinski models. In this work, we run a grid of models with different disk radial velocity dispersion σ_R , disk scale height z_d , number of particles N , and disk mass M_D . We analyzed the growth of spiral structures by using one and two dimensional Fourier Transform (FT1D and FT2D). The FT's give the amplitude, the number of arms, and the pitch angle of a particular spiral structure.

The FT1D was a powerful tool in order to understand the growth of the spiral structures. The results of the FT1D show us that the spiral structures emerge in the intermediate portion of the disk, where initially the Q parameter reaches its minimal value and these structures grow towards the outer parts of the disk with more intensity than they grow inwards, due to the steep increment of Q towards smaller radii.

The plots of the FT2D amplitude as a function of time and pitch angle show that *the general morphology of our modeled galaxies is due to the superposition of structures with different values of p , m , and angular velocity.*

We measured the angular velocity of all amplified patterns, and the results show that these patterns are very well confined between the main resonances given by the $\Omega \pm \kappa/m$ curves. Moreover, we found that different structures with either different or same mode m and frequency p , and different pattern speeds can evolve in the same region of the disk at the same time. Therefore,

it is important to note that very often two or three different spiral structures can coexist in the same region of the disk.

Masset & Tagger (1997) show signature of non-linear coupling between the bar and spiral waves, or between spiral waves from modes $m = 0$ to $m = 4$. Another similar frame is present by Sellwood (2011) where he showed that the bisymmetric spirals are not a single long-lived pattern, but the superposition of three or more waves can grow and decay with time. On the other hand, we have shown that not only the spirals can overlap with different mode m , but also they can overlap with different frequency p . Thus, the general morphology of our modeled galaxies is then due to the superposition of structures with different values for p , and m , i.e., different pitch angle and number of arms.

We have again to remark that the mass ratios M_D/M_G , M_B/M_G , M_H/M_G , and the initial condition between models with few and high number of particles are equals, but the mass of the particles are different. Therefore, the evolution of these models are affected by the noise (Sellwood 2003, Weinberg & Katz 2007a,b). For example, the bar in the model s37_z10M is formed earlier than in the models s37_z10MX, probably due to the same softening we used for all models. The noise is more incremented in models with few number of particles than those high number of particles. Therefore, it is clear that by adding more particles to the models the noise is reduced, then the apparition of a bar or spirals is delayed (Sellwood 2003). However, all models have similar behavior during all time which means that the general behavior of the models is more affected by the spiral and/or bar activity than the noise as exposed by Sellwood (2003).

Finally, we made an orbital analysis in the bar reference frame for those models where the bar was formed. We proposed a very simple geometrically classification, in which we classified three types of orbits as follows: compacts, along the bar, and orbits trapped in the Lagrangian points L_4 and L_5 . Our main outcome was that after the bar formation, the compact like orbits increases their number to reach around 5% of the disk mass; the loop like orbits increases their number to achieved around 10% of the disk mass for all of these models; and the bar like orbits increases their number to attain around of 15%, 13%, 12% and 16% for fiducial, s37_z10MX, s37_z10MS, and s37_z10MXS models, respectively. *Thus, we have found that these three geometrically classified type of orbits, which are the ones trapped in the Lagrangian points L_3 , L_4 , and L_5 , encompass approximately one-third of the disk total mass for these barred models. Furthermore, a particle can change its orbit morphology during its evolution.*

Acknowledgments

The authors gratefully acknowledge the very constructive comments offered by the referee, Jerry Sellwood, which improved the presentation of this paper. The authors also acknowledge support from the Mexican foundation CONACyT for research grants.

REFERENCES

- Athanassoula, E., & Sellwood, J. A. 1986, MNRAS, 221, 213
Athanassoula, L. 2003, Galaxies and Chaos, 626, 313
Athanassoula, E. 2012, MNRAS, 426, L46
Athanassoula, E. 2014, MNRAS, 438, L81
Baba, J., Asaki, Y., Makino, J., et al. 2009, ApJ, 706, 471
Baba, J., Saitoh, T. R., & Wada, K. 2013, ApJ, 763, 46
Bertin, G., & Lin, C. C. 1996, Spiral Structure in Galaxies: a Density Wave Theory (Cambridge MA, MIT Press)
Binney, J., & Tremaine, S. 1987, Galactic Dynamics (Princeton NJ, Princeton University Press)
Bottama, R. 2003, MNRAS, 344, 358
Buta, R. J., Knapen, J. H., Elmegreen, B. G. et al. 2009, AJ, 137, 4487
Carlberg, R. G., & Freedman, W. L. 1985, ApJ, 298, 486
Chatzopoulos, S., Patsis, P. A., & Boily, C. M. 2011, MNRAS, 416, 479
Dehnen, W. 2000, Astronomische Gesellschaft Meeting Abstracts, 17, 1
Dehnen, W. 2002, Journal of Computational Physics, 179, 27
Dobbs, C. & Baba, J. 2014, PASA, 31, 35
D’Onghia, E., Springel, V., Hernquist, L., & Keres, D. 2010, ApJ, 709, 1138
D’Onghia, E., Vogelsberger, M., & Hernquist, L. 2013, ApJ, 766, 34
Foyle, K., Rix, H. W., Dobbs, C. L., Leroy, A. K., & Walter, F. 2011, ApJ, 735, 101
Fuchs, B., Dettbarn, C., & Tsuchiya, T. 2005, A&A, 444, 1
Fujii, M. S., Baba, J., Saitoh, T. R., et al. 2011, ApJ, 730, 109
Gauthier, J.-R., Dubinski, J., & Widrow, L. M. 2006, ApJ, 653, 1180
Gerin, M., Combes, F., & Athanassoula, E. 1990, A&A, 230, 37
Goldreich, P., & Lynden-Bell, D. 1965, MNRAS, 130, 125
Grand, R. J. J., Kawata, D., & Cropper, M. 2012a, MNRAS, 421, 1529
Grand, R. J. J., Kawata, D., & Cropper, M. 2012b, MNRAS, 426, 167
Julian, W. H., & Toomre, A. 1966, ApJ, 146, 810
Klypin, A., Valenzuela, O., Colín, P., & Quinn, T. 2009, MNRAS, 398, 1027
Kuijken, K., & Dubinski, J. 1994, MNRAS, 269, 13
Kuijken, K., & Dubinski, J. 1995, MNRAS, 277, 1341
Lin, C. C., & Shu, F. H. 1964, ApJ, 140, 646
Martínez-García, E. E., & González-Lópezlira, R. A. 2013, ApJ, 765, 105
Masset, F., & Tagger, M. 1997, A&A, 322, 442
Mata-Chávez, D., Gómez, G. C., & Puerari, I. 2014, MNRAS, 444, 3756
Meidt, S. E., Rand, R. J., & Merrifield, M. R. 2009, ApJ, 702, 277
Merritt, D., & Sellwood, J. A. 1994, ApJ, 425, 551
Merrifield, M. R., Rand, R. J., & Meidt, S. E. 2006, MNRAS, 366, L17
Minchev, I., & Famaey, B. 2010, ApJ, 722, 112
Okamoto, T., Isoe, M., & Habe, A. 2015, PASJ, 67, 63
Puerari, I., & Dottori, H. A. 1992, A&AS, 93, 469
Puerari, I., Block, D. L., Elmegreen, B. G., Frogel, J. A., Eskridge, P. B. 2000, A&A, 359, 932
Roca-Fàbrega, S., Valenzuela, O., Figueras, F., et al. 2013, MNRAS, 432, 2878
Romeo, A. 1998, A&A, 335, 922
Saha, K. & Elmegreen, B. G. 2016, ApJ 826, L21
Sellwood, J. A., & Carlberg, R. G. 1984, ApJ, 282, 61
Sellwood, J. A. 2000, Ap&SS, 272, 31

- Sellwood, J. A. 2003, *ApJ*, 587, 638
Sellwood, J. A. 2010, arXiv:1001.5430
Sellwood, J. A. 2011, *MNRAS*, 410, 1637
Sellwood, J. A. 2013, *ApJ*, 769, L24
Sellwood, J. A., & Binney, J. J. 2002, *MNRAS*, 336, 785
Sellwood, J. A. 2013, *Planets, Stars and Stellar Systems. Volume 5: Galactic Structure and Stellar Populations*, 923
Sellwood, J. A., & Carlberg, R. G. 2014, *ApJ*, 785, 137
Speights, J. C., & Westpfahl, D. J. 2012, *ApJ*, 752, 52
Tremaine, S., & Weinberg, M. D. 1984, *MNRAS*, 209, 729
Teuben, P. 1995, *Astronomical Data Analysis Software and Systems IV*, 77, 398
Toomre, A. 1981, in *Structure and Evolution of Normal Galaxies* (Cambridge University Press), 111
Valencia-Enríquez, D., & Puerari, I. 2014, *ASP Conference Series*, 480, 145
Wada, K., Baba, J., & Saitoh, T. R. 2011, *ApJ*, 735, 1
Weinberg, M. D., & Katz, N. 2007, *MNRAS*, 375, 425
Weinberg, M. D., & Katz, N. 2007, *MNRAS*, 375, 460

Diego Valencia-Enríquez, Ivânio Puerari and Leonardo Chaves-Velasquez: Instituto Nacional de Astrofísica, Óptica y Electrónica, Calle Luis Enrique Erro 1, Santa María Tonantzintla, 72840 Puebla, Mexico (E-mail: valencia@inaoep.mx, diegovalencia5@gmail.com).